Deep–Sea Research I 203 (2024) 104217

Contents lists available at ScienceDirect

Deep-Sea Research Part I

journal homepage: www.elsevier.com/locate/dsri

Sensitivity of the thermohaline circulation during the Messinian: Toward constraining the dynamics of Mediterranean deoxygenation

A.M. Mancini [a,*], R. Gennari [a], F. Lozar [a], M. Natalicchio [a], G. Della Porta [b], D. Bernasconi [a], L. Pellegrino [a], F. Dela Pierre [a], L. Martire [a], A. Negri [c]

[a] Earth Sciences Department, Università degli Studi di Torino, 10125, Torino, Italy
[b] Earth Sciences Department "A. Desio", Università degli Studi di Milano, 20133, Milan, Italy
[c] Department of Life and Environmental Science, Università Politecnica delle Marche, 60122, Ancona, Italy

ARTICLE INFO

Keywords:
Calcareous nannofossil
Carbon and Oxygen stable isotopes
Anoxia
Foraminifers
Paleoenvironmental reconstruction
Climate Change

ABSTRACT

During the Messinian, the sensitivity of the Mediterranean Basin to ecosystem perturbation was enhanced in response to the progressive restriction of water exchange with the Atlantic Ocean. The widespread deposition of organic-rich layers (i.e. sapropel) during the Messinian testifies the perturbation of the carbon and oxygen cycles; indeed, these sediments were deposited under conditions of oxygen starvation, presumably in response to a periodic deterioration of the thermohaline circulation strength. Disentangling the causes, the effect and magnitude of the thermohaline circulation weakening during the geological past is crucial for better constraining present and near-future deoxygenation dynamics in the Mediterranean region under the current climate warming. For this purpose, we investigate a Messinian sapropel-bearing succession cropping out at Monte dei Corvi (Ancona, central Italy) with mineralogical, petrographic, micropaleontological and stable Carbon and Oxygen isotopic analyses. We show that sapropel layers were deposited in response to an increase of the sea surface buoyancy, which hampered the thermohaline circulation and thus the oxygenation of bottom water, in turn affecting the bioturbating organisms. Within the lithological cycle, the recovery of an efficient thermohaline circulation is recorded by thin packstone layers underlying the marly limestone/marlstone, which record intense bottom currents. The marly limestone/marlstone accumulated during periods of intense primary productivity and organic carbon export to the sea bottom, which promoted bottom hypoxia but not organic matter preservation. We infer that these lithological changes resulted from variations in the Adriatic Deep Water formation system, controlled by precession-driven climatic and oceanographic changes.

By integrating previously published Sea Surface Temperature (SST) with new isotopic and mineralogical data, we show that variations in Sea Surface Salinity (SSS) were the leading factor controlling sapropel deposition, minimizing the role of primary productivity. The SSTs characterizing the sapropel deposits are close to the range of those projected in the Eastern Mediterranean at the end of this century under climate warming. In this scenario, future warming will be coupled with SSS increase, which will counteract the density loss provided by temperature, making the bottom deoxygenation in the Eastern Mediterranean abysses unlikely. However, additional forcing, such as winter heat waves and eutrophication, could contribute to negatively affecting the Mediterranean oxygen balance and should be considered in model-based projections.

1. Introduction

The Mediterranean region is considered one of the most sensitive regions to climate change on Earth; for this reason it has been referred to as a climate change "hot-spot" (Giorgi, 2006). Warming and drying were recorded during the last decades and these trends are projected to further exacerbate in the next future (IPCC, 2021). The warming trend is impacting the thermohaline circulation strength (Somot et al., 2006), with possible repercussions on the oxygen renewal in the deep-water masses (Diaz and Rosenberg, 2008). The Mediterranean thermohaline circulation mostly relies on cold wind stress and evaporation mechanisms; the lighter (less saline but colder) surface water entering the Gibraltar Strait and flowing toward the Eastern Mediterranean progressively becomes saltier and warmer. In the Levantine Basin during

* Corresponding author.
E-mail address: alanmaria.mancini@unito.it (A.M. Mancini).

https://doi.org/10.1016/j.dsr.2023.104217
Received 25 August 2023; Received in revised form 16 November 2023; Accepted 13 December 2023
Available online 21 December 2023

winter the cold and dry wind decreases the temperature and increases the salinity of surface water, favoring vertical convection and the formation of the Levantine Intermediate Water (LIW), which flows west-ward between 150 and 600 m depth (Rohling et al., 2015 and reference therein). Similarly, in the Northern Adriatic, the winter cold wind decreases the temperature of surficial waters favoring their sink; this cold water flows south-ward at the Adriatic bottom and is mixed with the LIW that comes from the Otranto Sill (Rohling et al., 2015). The mixing between these two water masses promotes the formation of the Adriatic Deep Water (ADW), which resides below the LIW and represents the major contribution of deep-water renewal in the Eastern Mediterranean abysses, assuring oxygen supply at the bottom.

Starting from the Langhian (Taylforth et al., 2014; Athanasiou et al., 2021), the Mediterranean experienced deoxygenation events related to a strong reduction, or even a complete stop, of the thermohaline circulation (Stratford et al., 2000; De Lange et al., 2008; Rohling et al., 2015), coupled with an increase in marine primary productivity (Rohling et al., 2015; Blanchet et al., 2021). These paleoceanographic changes caused most of the deoxygenation events in the geological history of the Mediterranean and were mostly related to changes in continental runoff, temperature and sea level (Rohling et al., 2015 and reference therein). A strong temporal correlation exists between the Mediterranean deoxygenation events and precession minima/eccentricity maxima, since these orbital parameters control the incoming solar energy and promote the northward migration of the monsoon rain belt over North Africa, therefore increasing fluvial discharge in the Eastern Mediterranean Basin mostly through the Nile River (Rossignol-Strick et al., 1982; Hennekam et al., 2014; Rohling et al., 2015). The enhanced freshwater input into the Mediterranean Basin increased the buoyancy of surface waters, thus promoting density stratification of the water column and hampering deep water renewal (Rohling et al., 2015). These events are recorded by dark layers, termed sapropels, which are marine sediments enriched in organic carbon (Kidd et al., 1978), which punctuated the Eastern Mediterranean sedimentary record of the last 15 My (Taylforth et al., 2014; Athanasiou et al., 2021). Sapropel deposition was induced by sharp perturbations of the oxygen and carbon cycles; indeed, these layers record organic matter preservation in response to bottom oxygen deficiency. During the Messinian, sapropel deposits are more widespread and frequent with respect to the rest of the Mediterranean geological record, because the tectonic shallowing of the paleo-Gibraltar gateway reduced the water exchange with the Atlantic Ocean (Roveri et al., 2014; Flecker et al., 2015) and increased the sensitivity of thermohaline circulation to freshwater input, hence promoting the weakening of the thermohaline circulation and bottom oxygen delivery (Kouwenohven and Van der Zwaan, 2006; Mancini et al., 2020; Bulian et al., 2022). The freshwater input from the African rivers was coupled with the Paratethys freshwater spill (Gladstone et al., 2007), which further enhanced the density loss of surface water during precession minima in the Eastern Mediterranean. These characteristics make the Messinian sedimentary succession an excellent case study for unraveling the causes and the effects of deoxygenation events in the geological past and for comparing such past environmental perturbations with the current and near-future scenarios of climate change.

A sapropel-bearing Messinian succession exposed in the Northern Apennines (Conero Riviera, Ancona, Italy) is investigated using a high-resolution multidisciplinary approach, encompassing mineralogical, sedimentological, micropaleontological, and carbonate stable Oxygen and Carbon isotope data. The objective is to unravel the environmental conditions responsible for Messinian sapropel deposition in the Adriatic Basin and compare these past perturbations with those projected in the near future under the influence of climate change scenarios in the Mediterranean Basin.

2. Geological setting

The studied section is located south of Ancona and is exposed along the shoreline between Monte dei Corvi and Mezzavalle beach (43° 34′N, 13° 34′E; Fig. 1). This area pertains to the central sector of the modern foredeep basin and foreland ramp of the northern Apennine belt (Roveri et al., 2005). The sedimentary succession is almost continuous from the Aquitanian to the Messinian (Hilgen et al., 2003). The Messinian succession was deposited in the outer northern Apennine foredeep (Roveri et al., 2005) and is composed of a pre-evaporitic, a syn-evaporitic and a post-evaporitic unit (Roveri et al., 2005; Iaccarino et al., 2008). The ~20 m thick pre-evaporitic unit is referred to as the "Euxinic shale interval" and shows a precession-driven cyclic stacking pattern evidenced by couplets of dark, organic-rich marlstone (here referred as sapropel) and white/light grey limestone or marlstone (Hüsing et al., 2009; Di Stefano et al., 2010). This interval was deposited at a water depth of 300–400 m (outer shelf/upper slope, Iaccarino et al., 2008) and was characterized by hemipelagic sedimentation in the outer foredeep setting (Fig. 1; Roveri et al., 2005). The syn-evaporitic unit is represented by resedimented gypsum deposits partially covered by a landslide that is overlain by ~170 m of post-evaporitic deposits (Bertini and Menichetti, 2015). The Messinian succession ends with a complex biocalcarenitic sedimentary body, termed Trave, which marks the transition to the Pliocene sediments. The studied section pertains to the pre-evaporitic Messinian "Euxinic shale interval" and was referred to as "extension Monte dei Corvi Beach" in previous studies (Hüsing et al., 2009; Di Stefano et al., 2010). The age model proposed by Hüsing et al. (2009) was applied, which has been defined according to biostratigraphic, magnetostratigraphic and cyclostratigraphic data. For this study, 4 lithological cycles (from 253 to 256 according to Hüsing et al., 2009) were analyzed, with an inferred age of 6.553 to 6.479 Ma. A total of 40 samples were collected, with a mean stratigraphic spacing of 5 cm (Fig. 2).

3. Materials and methods

3.1. Petrographical, geochemical and micropaleontological analyses

Among the 40 samples collected, thirteen polished thin sections were prepared for optical and cathodoluminescence microscope analyses; a CITL 8200 mk3 equipment operated at 15–17 kV and 350–500 mA was used. Scanning Electron Microscope (SEM) and energy-dispersive X-ray spectroscopy (EDS) analyses were performed on the same carbon-coated thin sections for semiquantitative elemental analyses and backscattered electron imagery (BSEI) using a JSM-IT300LV equipped with EDS Oxford Instruments Link Systems (Department of Earth Sciences, University of Turin). Elemental compositional maps were obtained from selected areas using the software Inca. SEM analyses were also performed on 36 freshly broken chips for morphological investigations, along with a qualitative micropaleontological observation (Fig. 2) to estimate the abundance and preservation of benthic and planktic foraminifers and calcareous nannofossils. Four standard smear slides were prepared and quantitatively investigated to assess the calcareous nannofossil assemblages. These samples were observed at the optical microscope at 1250x and at least 400 specimens were identified for the calculation of the relative abundance.

Carbon ($\delta^{13}C$) and Oxygen ($\delta^{18}O$) stable isotope analyses were conducted on 26 powdered samples (Fig. 2) using an automated carbonate preparation device (Gasbench II) and a Thermo Fisher Scientific Delta V Advantage continuous flow mass spectrometer at the University of Milan. The powders were reacted with >99% orthophosphoric acid at 25° and 70 °C with the aim to distinguish the possible contribution of the different carbonate minerals (calcite and dolomite). Carbon and oxygen isotope values are expressed in the conventional delta notation calibrated to the Vienna Pee-Dee Belemnite (V-PDB) scale by the international standards IAEA 603 and NBS-18. Analytical reproducibility was better than ±0.1‰ for both $\delta^{18}O$ and $\delta^{13}C$ values. In order to highlight differences in the isotopic composition between bulk calcite and calcareous nannofossils calcite, 4 samples (sb2bot 0–2; sb2bot 6–7; sb10

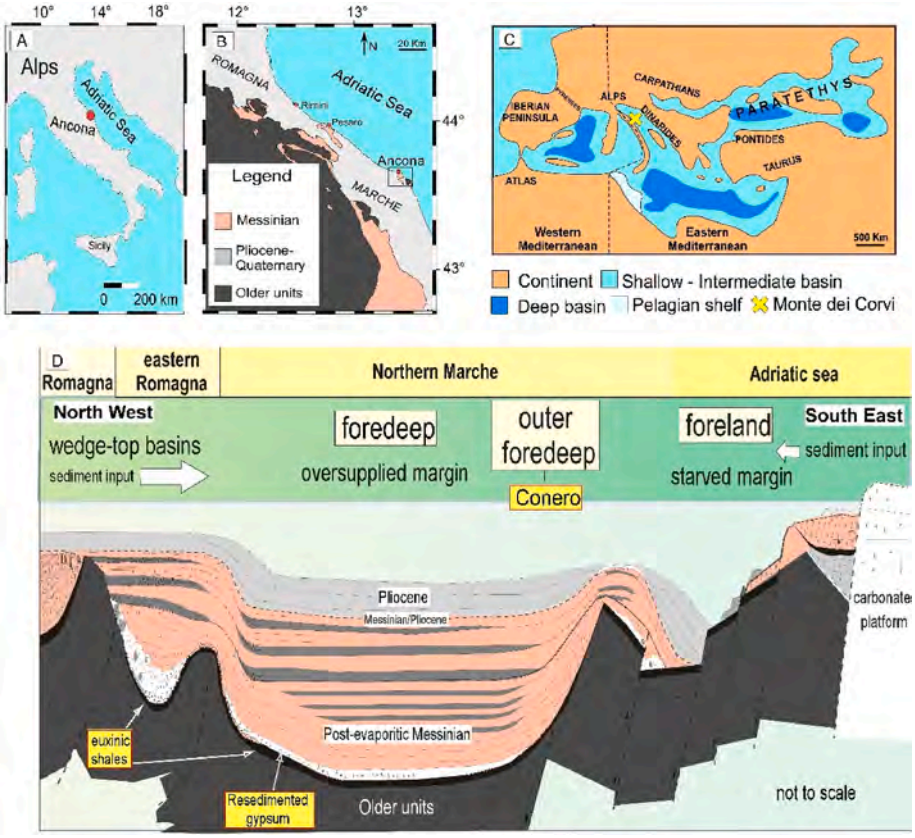

Fig. 1. Geological and paleogeographic map of the studied area and general stratigraphic scheme of the late Neogene deposits. A and B: Location and simplified geological map of the studied area. The studied section is indicated by the black square in B. C: Paleogeographic reconstruction of the Mediterranean during the early Messinian. Modified after Popov et al. (2004). D: Stratigraphic architecture of the Messinian deposits of the Apennine foredeep with location of the studied area (Conero). Modified after Roveri et al. (2005).

6–7; sb17 8–9; Fig. 2) were gently crushed to obtain ~1 mm of grain size, the powder and grains obtained were successively sieved at 45 μm in order to concentrate the calcareous nannofossils, in agreement with previous paleoceanographic studies (Anderson and Steinmetz, 1981; Steinmetz, 1994; among others). Successively, the fraction <45 μm was analyzed with the same procedure applied to the bulk sediment. These samples were chosen because their assemblages show a different taxonomic diversity (see paragraph 4.1).

The Total Organic Carbon (TOC, wt%) content was obtained from 10 powdered samples that were first reacted with HCl at 18% and cleaned for removing excess of acid; then, the decarbonized material was embedded in thin pellets and analyzed with Elemental Analyzer Flash2000 (Thermo Fisher) at the University of Milan.

Ten powdered samples were processed with the X-Ray Powder Diffraction (XRPD) (Fig. 2) at the University of Turin. The phase composition was determined by X-ray Powder Diffraction measurements using a para-focusing geometry Rigaku Miniflex 600, with Cu-Kα incident radiation and operating at 40 kV–15 mA. The diffractometer is equipped with a DTex 250 detector and an optic configuration consisting of a fixed divergence slit (1/2°) and an anti-scatter slit (1/2°). XRPD patterns were collected on powdered samples between 3° and 70° 2θ, with a 2θ-step size of 0.01 and scan speed of 1°/min, using a side-loading zero-background sample holder. The phase content was inferred by Rietveld analysis, using high-purity ZnO as an internal standard (10 wt %). Data refinements were carried out by the software GSAS-II (Toby and Von Dreele, 2013). The Rietveld strategy involved the refinement of 15 Chebyshev polynomial background coefficients, 2θ-zero parameter, cell parameters, phase fractions, isotropic crystal size, isotropic microstrain of each phase and preferential orientation Mach-Dollase coefficients, when necessary. The PDF-4 2020 database enabled the phase identification.

3.2. Salinity reconstruction

$\delta^{18}O$ of biogenic calcite are a function of the temperature and the oxygen isotopic composition of seawater (usually referred to as $\delta^{18}O_{SW}$) in which calcite precipitates. In living coccolithophores, the fractionation factor for oxygen isotopes between water and calcite shows a large temperature dependence (Dudley et al., 1986; Steinmetz, 1994; Hermoso, 2014). However, because of the "vital effect" on isotopic fractionation, different taxa show a $\delta^{18}O$ offset with respect to the isotopic composition expected from equilibrium fractionation during the precipitation of calcite at a given temperature (Dudley et al., 1986; Hermoso, 2014, Fig. 3). For this reason, Dudley et al. (1986) and Hermoso (2014) coined the terms "heavy group", "equilibrium group" and "light group" to describe the oxygen isotope departure from the equilibrium of different taxa. Based on the assumption that most of the calcite in the analyzed samples derives from well-preserved calcareous nannofossils (see Result section), the $\delta^{18}O$ values were converted into sea surface salinity (SSS) by using different paleotemperature equations and applying the alkenone-based sea surface temperature (SST) estimation provided by Tzanova et al. (2015) on the same section. Being the alkenone a by-product of certain calcareous nannofossil taxa, the $\delta^{18}O_{nannofossils}$ is preferable over $\delta^{18}O_{foraminifers}$ for the salinity evaluation, because it reduces inconsistency between proxy sources, such as differences in the habitat of the living organism. To take into account the vital effect of different calcareous nannofossils, we applied the paleotemperature equation of "heavy" (y = 4.34–0.20x), "equilibrium" (approximated by *Helicosphaera carteri*: y = 3.53 + 0.28x) and "light" (y = −1.37-0.12x) coccolithophore groups according to Dudley et al.

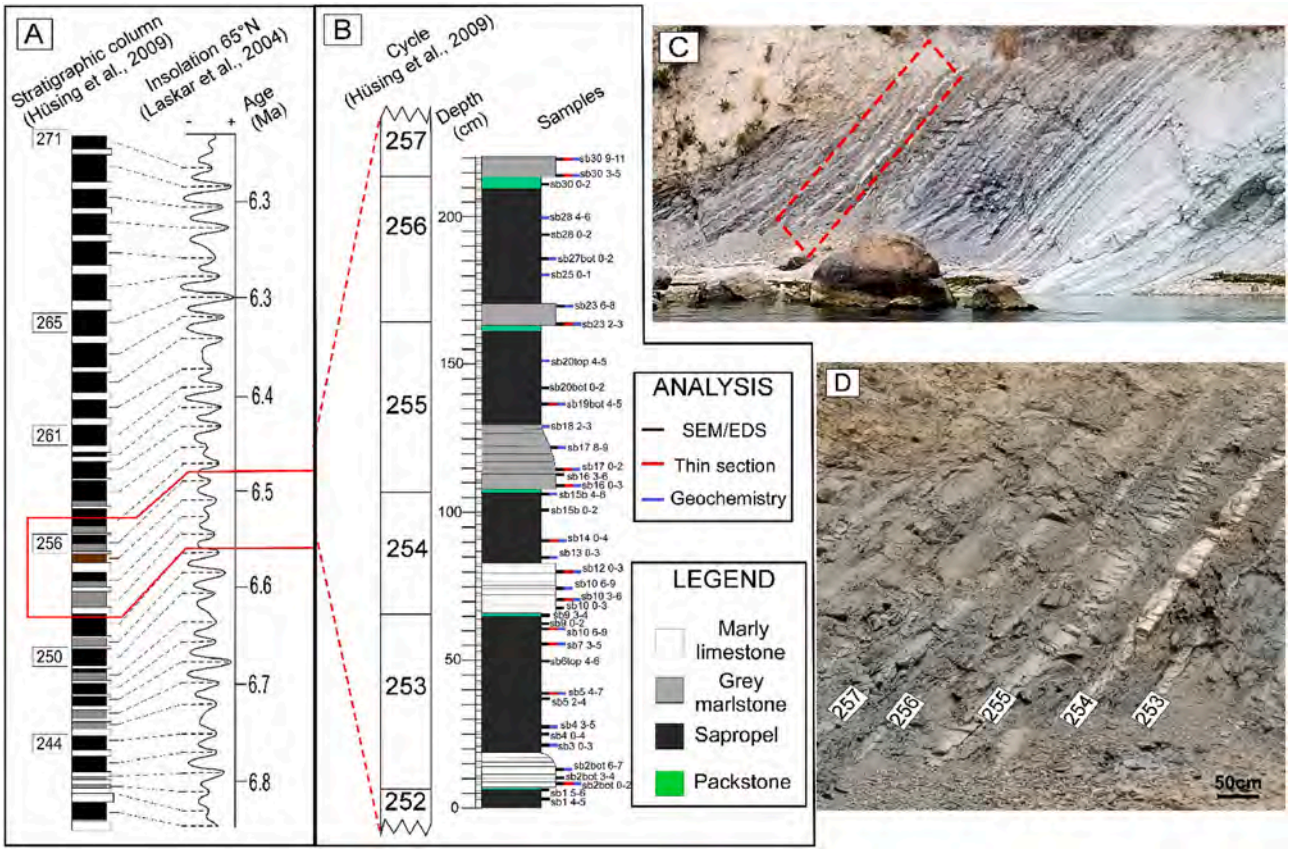

Fig. 2. A: Stratigraphic column of Monte dei Corvi section; numbers on the left refer to the identified cycles (after Hüsing et al., 2009); The red polygon shows the studied part of section. B: The studied part of the section with detail on lithology and sample position. C: Outcrop view of the section showing the sampled interval (red dashed line square). D: Close-up of the studied section with labeling of the cycles.

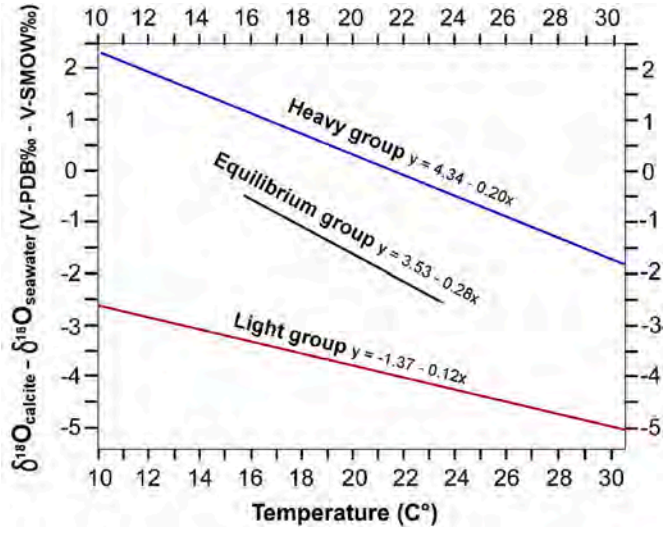

Fig. 3. Plot of $\delta^{18}O_{calcite}$ - $\delta^{18}O_{seawater}$ versus the growth temperature of different coccolith taxa grouped according to their vital effect behavior. Light and heavy groups are defined by Dudley et al. (1986), and the equilibrium by Ziveri et al. (2003) and Hermoso (2014).

(1986) and Ziveri et al. (2003), where y is $\delta^{18}O_{calcite}$ - $\delta^{18}O_{sw}$ (‰ V-PDB – ‰ V-SMOW) and x is the temperature in °C (Fig. 3). Successively, we calculated the average between the 3 equations along with standard deviation in order to account the possible contribution of nannofossils with different vital effect. In all equations, the SST was derived from the values provided by Tzanova et al. (2015), which were recalculated to accommodate the different sampled stratigraphic levels by linear interpolation using the sapropel mid-point as tie-points (insolation maxima; Hilgen et al., 2003) and applying a constant sedimentation rate. The extrapolated SST and the calculated age for each sample are reported in Table 1. Finally, by removing the temperature influence on $\delta^{18}O_{calcite}$, we achieved $\delta^{18}O_{SW}$. Changes in the continental ice volume also affect the global $\delta^{18}O_{SW}$, therefore it is necessary to estimate the contribution of this component to obtain regional salinity change indications (Vasiliev et al., 2019; Kontakiotis et al., 2022; Pilade et al., 2023). With this aim, we accounted for the change in the global ice volume by correcting the $\delta^{18}O_{SW}$ with the Messinian record of sea-level change (Miller et al., 2011) and applying a 0.008‰ increase per meter of sea level lowering (Siddall et al., 2003); successively, this value was subtracted from the $\delta^{18}O_{SW}$ to obtain the regional ice volume free $\delta^{18}O_{SW}$ ($\delta^{18}O_{iivf\text{-}SW}$). The $\delta^{18}O$ value was then converted to absolute SSS using the modern $\delta^{18}O_{SW}$ – salinity relationship for the Mediterranean Sea ($\delta^{18}O_{sw}$ = 0.41*SSS – 14.18) (Kallel et al., 1997). However, the obtained SSS should be considered with caution, as this conversion was calibrated for a narrow salinity range (~35‰–39‰) (Kallel et al., 1997) and the assumed constant relationship between SSS and $\delta^{18}O_{SW}$ changed in the past (LeGrande and Schmidt, 2011), especially during the Messinian, which was characterized by large variations in freshwater input and evaporation. In view of all these uncertainties, our SSS reconstructions are intended as an estimation of salinity trend and presented for illustrative and comparative scope.

From the SSS and SST estimates, the density variation of the surface water was calculated assuming constant pressure according to the international thermodynamic equation of seawater [(d = d (Sa, t, p)], where Sa is the absolute salinity, t is the measured temperature and p is

Table 1
Results of the calculated SSS and surficial density (for detail, see paragraph 3.2) with the age of the samples, the interpolation with the alkenone-based SST reconstruction (Tzanova et al., 2015), the global sea-level variation during the Messinian (Miller et al., 2011), the calculated $\delta^{18}O_{ivf\text{-}sw}$ and the propagated standard deviation accounted for different paleotemperature equations used.

			δ18Osw (‰)									
Age (kyr)	SST (C°)	$\delta^{18}O_{bulk}$ (‰)	Heavy group	Equilibrium group	Light group	Average 3 groups	Sea level	$\delta18O_{ivf\text{-}sw}$ (‰)	Sum St. dev.	SSS (‰)	St. dev.	Density (Kg/m3)
6479.3	25.1	0.8	1.6	4.4	5.3	3.7 ± 1.6	-4.0	3.7	1.6	43.7 ± 4.7	4.7	1029.89 ± 2.92
6479.9	25.45	1.1	1.9	4.8	5.6	4.1 ± 1.6	-4.21	4.1	1.6	44.5 ± 4.7	4.7	1030.44 ± 2.91
6484.8	25.05	-2.6	-1.9	0.9	1.8	0.3 ± 1.6	-4.6	0.3	1.6	35.2 ± 4.7	4.7	1023.52 ± 2.91
6489.7	24.4	-2.9	-2.3	0.5	1.5	-0.1 ± 1.6	-3.8	-0.1	1.6	34.3 ± 4.7	4.7	1022.99 ± 2.93
6491.9	24.7	-2.9	-2.2	0.5	1.5	-0.1 ± 1.6	-4.7	-0.1	1.6	34.4 ± 4.7	4.7	1022.99 ± 2.92
6495.7	25.32	1.2	1.9	4.8	5.6	4.1 ± 1.6	-5.0	4.1	1.6	44.6 ± 4.7	4.7	1030.54 ± 2.92
6497.8	25.6	2.3	3.1	6.0	6.8	5.3 ± 1.6	-6.1	5.3	1.6	47.5 ± 4.7	4.7	1032.67 ± 2.91
6504.9	25.43	-0.9	-0.1	2.8	3.6	2.1 ± 1.6	-8.0	2.1	1.6	39.7 ± 4.7	4.7	1026.78 ± 2.91
6510.7	24.8	-0.6	0.1	2.9	3.8	2.3 ± 1.6	-8.4	2.2	1.6	40.1 ± 4.7	4.7	1027.25 ± 2.93
6512.8	24.9	1.7	2.4	5.2	6.1	4.5 ± 1.6	-8.45	4.5	1.6	45.6 ± 4.7	4.7	1031.44 ± 2.93
6514.9	25.05	2.4	3.1	5.9	6.8	5.3 ± 1.6	-4.9	5.3	1.6	47.5 ± 4.7	4.7	1032.81 ± 2.93
6517.0	25.3	1.9	2.6	5.4	6.3	4.8 ± 1.6	-4.9	4.8	1.6	46.3 ± 4.7	4.7	1031.79 ± 2.92
6520.0	25.6	1.1	1.9	4.8	5.6	4.1 ± 1.6	-4.98	4.1	1.6	44.6 ± 4.7	4.7	1030.45 ± 2.91
6521.0	25.71	-5.7	-4.9	-2.0	-1.2	-2.7 ± 1.6	-5.0	-2.7	1.6	28.0 ± 4.7	4.7	1017.81 ± 2.88
6527.4	25.95	-5.3	-4.4	-1.5	-0.7	-2.2 ± 1.6	-4.9	-2.2	1.6	29.2 ± 4.7	4.7	1018.70 ± 2.87
6529.4	25.8	-4.2	-3.3	-0.4	0.3	-1.1 ± 1.6	-4.0	-1.1	1.6	31.8 ± 4.7	4.7	1020.63 ± 2.85
6531.6	25.1	2.2	2.9	5.7	6.6	5.03 ± 1.6	-3.0	5.0	1.6	46.8 ± 4.7	4.7	1032.31 ± 2.93
6534.0	24.48	2.5	3.0	5.8	6.8	5.2 ± 1.6	-1.0	5.2	1.6	47.2 ± 4.7	4.7	1032.81 ± 2.95
6534.8	24.4	1.8	2.4	5.1	6.1	4.6 ± 1.6	-1.2	4.6	1.6	45.7 ± 4.7	4.7	1031.65 ± 2.95
6537.7	24.9	-2.1	-1.4	1.4	2.3	0.8 ± 1.6	-2.6	0.8	1.6	36.4 ± 4.7	4.7	1024.46 ± 2.92
6539.3	25	-3.2	-2.5	0.3	1.2	-0.4 ± 1.6	-4.9	-0.4	1.6	33.7 ± 4.7	4.7	1021.62 ± 2.31
6544.1	25.38	-4.4	-3.6	-0.8	0.0	-1.5 ± 1.6	-8.5	-1.5	1.6	31.0 ± 4.7	4.7	1020.21 ± 2.89
6547.6	24.7	-3.0	-2.3	0.5	1.4	-0.1 ± 1.6	-9.3	-0.1	1.6	34.3 ± 4.7	4.7	1022.90 ± 2.92
6549.7	25	-2.6	-1.8	1.0	1.9	0.4 ± 1.6	-9.3	0.4	1.6	35.4 ± 4.7	4.7	1023.68 ± 2.91
6551.7	25.5	1.8	2.6	5.5	6.3	4.8 ± 1.6	-8.8	4.8	1.6	46.3 ± 4.7	4.7	1031.75 ± 2.91
6553.3	24.8	1.7	2.4	5.2	6.1	4.6 ± 1.6	-7.6	4.6	1.6	45.7 ± 4.7	4.7	1031.59 ± 2.94

the pressure of seawater (Intergovernmental Oceanographic Commission, 2015).

4. Results

4.1. Sedimentological, petrographic, and micropaleontological features

The studied succession is typified by a cyclic stacking pattern. The cycles were usually described as couplets (Hüsing et al., 2009; Di Stefano et al., 2010); however, detailed field observations revealed that a packstone layer occurs between the marly limestone/marlstone and the sapropels (Figs. 2 and 5). The calcareous nannofossil assemblage in the quantitatively analyzed samples is dominated by *Umbilicosphaera jafari*, with a relative percentage spanning from 48% to 98% (Fig. 4). The full calcareous nannofossil assemblage is reported in the supplementary materials.

4.1.1. Packstone

This lithology forms thin (1–4 cm thick) brown/dark layers composed of sand-sized foraminifers and green minerals attributable to glauconite (Fig. 5), while the matrix is represented by carbonate mud mixed with clay. The base of each layer is an erosional surface cutting the underlying sapropel. The lower part of the layers is usually poorly cemented and grades into a strongly cemented limestone at the top (Fig. 5). Based on the petrographic and sedimentological features, 2 levels (A and B) can be distinguished from the base to the top.

- Level A is characterized by high contents of foraminifers associated with varying amounts of glauconite (Fig. 5). The tests of foraminifers are consistently filled with sparry calcite (Fig. 4), with different cathodoluminescence brightness (bright orange) with respect to the matrix (non-luminescent brown) (Fig. 5) due to a different trace element (Mn, Fe) content, pointing to different phases of precipitation.
- Level B is characterized by a pervasive bioturbation. The burrows are 0.5–5 mm in diameter, oriented parallel to the bedding, and filled with pyrite, barite, calcite and gypsum.

4.1.2. Marly limestone/marlstone

Based on the percentage of calcite (see paragraph 4.2), the whitish/grey layers interbedded with the sapropel are either marly limestone or marlstone (Fig. 2). These beds span from 7 to 20 cm in thickness and are

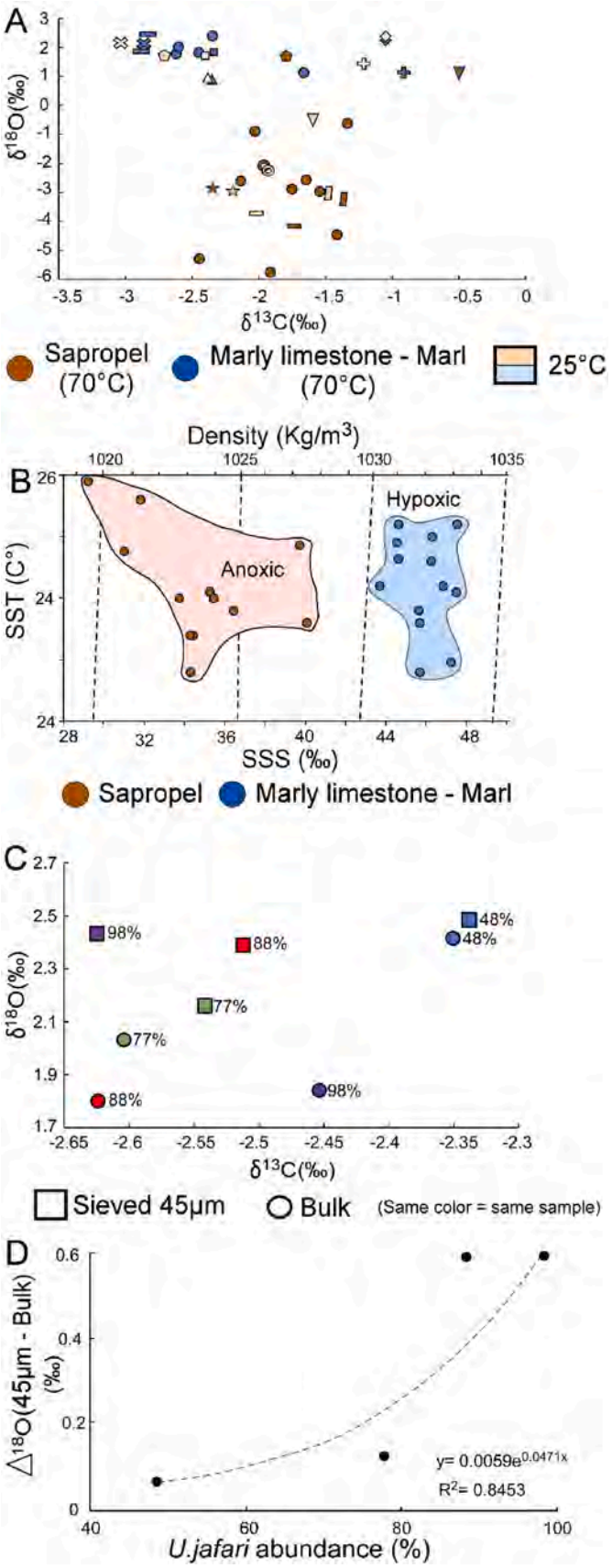

(caption on next column)

Fig. 4. Scattered plots of the measured $\delta^{13}C_{calcite}$, $\delta^{18}O_{calcite}$ values and *U. jafari* abundance.
A: Plot showing the distribution of $\delta^{13}C_{calcite}$ and $\delta^{18}O_{calcite}$ values in different lithologies and with different procedures (treatment at 25° or 70 °C). The same symbol refers to the same sample.
B: Density plot reconstructed from the SSS and SST of the different lithologies.
C: Comparison between the $\delta^{13}C$ and $\delta^{18}O$ values measured in the bulk sediment and sieved at 45 μm. Same color refers to same sample.
D: Plot showing the exponential relationship between the differences in the $\delta^{18}O_{45\mu m}$ and the $\delta^{18}O_{bulk}$ and the *U.jafari* relative abundance. The equation of the relationship and the linear relationship coefficient R^2 are shown in the right lower corner.

usually laminated, showing the alternation of grey-white and brown-dark laminae (Fig. 5). The white laminae are 150–600 μm thick and are composed of closely packed fecal pellets (average size ~200 μm) rich in calcareous nannofossils (Figs. 4–6). In some beds (i.e. cycles 253 and 254) fecal pellets are made of monospecific or oligospecific calcareous nannofossil assemblages of the taxon *U. jafari*. Pyrite and terrigenous grains (the latter only in cycles 255 and 256) are also present as minor components (Fig. 5). The brown-dark laminae mostly consist of fine-grained terrigenous material and pyrite grains (Fig. 5), as revealed by EDS analysis. Calcareous nannofossils are instead less abundant compared with the grey-white lamina. The foraminifer assemblage is dominated by poorly preserved benthic foraminifers filled with sparry calcite of diagenetic origin (Figs. 5 and 6).

4.1.3. Sapropel

Sapropel layers are 20–50 cm thick and are finely laminated, with grey-white laminae (50–600 μm thick) mostly made up of peloids and fecal pellets, alternated with black-brown laminae (50–200 μm thick) composed of silt-sized terrigenous and pyrite grains. Foraminifers are scarce to abundant, and the assemblage is dominated by well-preserved planktic specimens, showing intact and well-preserved walls and empty chambers (Fig. 6). Calcareous nannofossils are less abundant compared to the marly limestone/marlstone samples.

4.2. Mineralogy and geochemistry

The mineralogical composition of the samples expressed in percentage is reported in Fig. 7. Overall, the marly limestone/marlstone shows higher calcite contents and lower pyrite, clay, and dolomite contents with respect to sapropel. The carbon and oxygen stable isotope analyses performed with acid digestion at 25 °C and 70 °C show similar values (Fig. 4). The $\delta^{18}O$ values obtained at 70 °C are consistently higher in the marly limestone/marlstone (from 0.8‰ to 2.4‰) and lower in the sapropel (from −5.7‰ to −0.6‰) (Fig. 7). The $\delta^{13}C$ values obtained at 70 °C span from −2.8‰ to −0.5‰ (Fig. 7). The calcite fraction of the sieved samples is dominated by well-preserved calcareous nannofossils (Fig. 6). The sieved samples show similar $\delta^{18}O$ values of the bulk sediment samples (Fig. 5), with deviation in the range of 0.05‰–0.60‰ (Fig. 4). The TOC contents of the studied samples span from 0.9% to 3.1% (Fig. 7); on average the sapropel and the marly limestone/marlstone show TOC content of 2.0% and 0.8%, respectively.

4.3. The reconstructed $\delta^{18}O_{SW}$ and SSS estimation

The calculated $\delta^{18}O_{SW}$ obtained using the different paleotemperature equations and the correlation between sea level and SST changes are given in Table 1. The average of the $\delta^{18}O_{ivf\text{-}SW}$ spans from −2.7 ± 1.6‰ to 5.3 ± 1.6‰, (Table 1) with higher values recorded in the marly/limestone-marlstone layers and lower values in the sapropel. The calculated SSS spans from 28.0‰ ± 4.7‰ (sapropel of cycle 254) to 47.5‰ ± 4.7‰ (marlstone of cycle 255) and shows an evident cyclical pattern related to the lithology (Figs. 4 and 7). Sapropel shows lower SSS values (average 34.1‰) than the marly limestone/marlstone (average

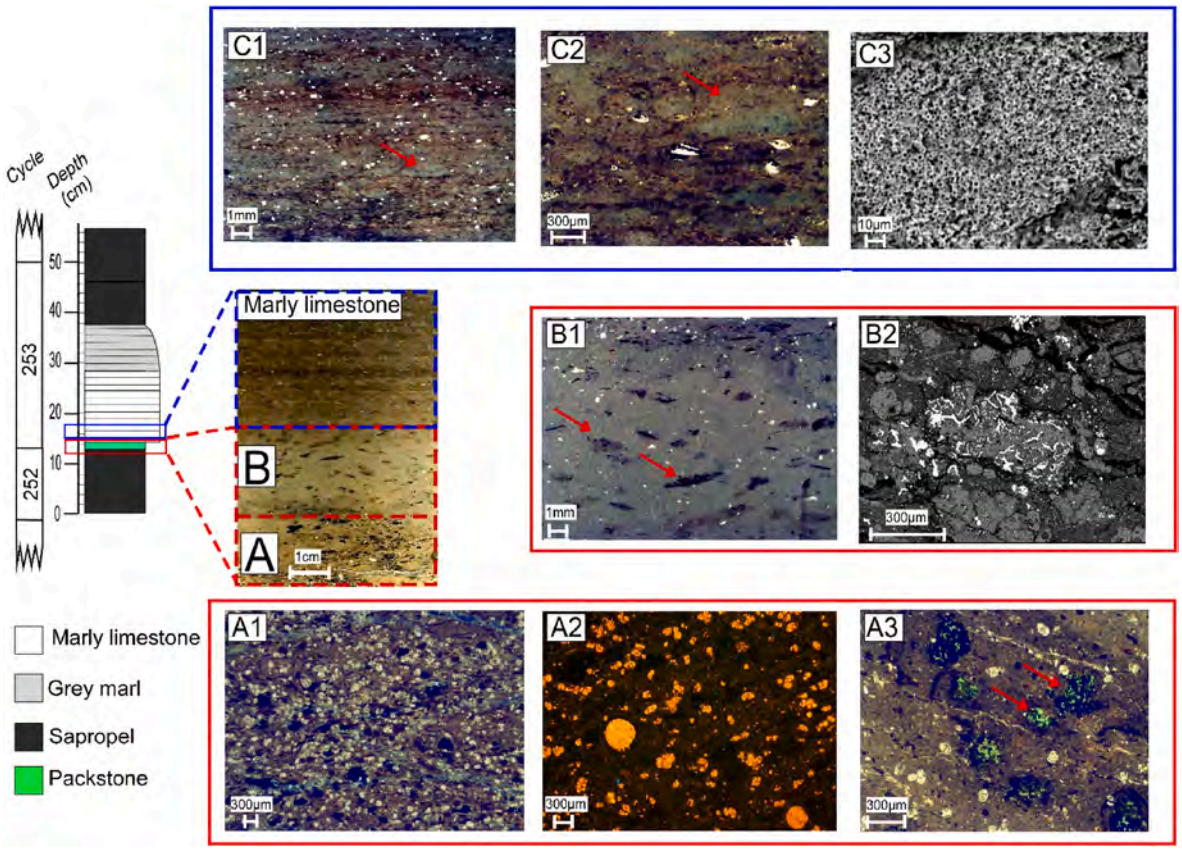

Fig. 5. Thin section photomicrographs of the packstone to marly-limestone transition. Based on petrographic and sedimentological features, the packstone layer is divided into 2 distinct levels. Level A shows high abundance of foraminifers (A1 and A2) and glauconite (red arrows in A3). Note that the sparry calcite foraminifer infill shows a different luminescence with respect to the matrix when inspected with cathodoluminescence (A2). Level B is characterized by intense bioturbation (red arrows in B1). Burrows are filled with pyrite (B2). The marly limestone shows the alternation of whitish and brown laminae (C1 and C2). Whitish laminae are composed of fecal pellets with a monospecific calcareous nannofossil assemblage (red arrows in C1 and C2, magnified at the SEM in C3). A1, A3, B1, C1 and C2: optical microscope photomicrographs; A2: cathodoluminescence photomicrograph; B2 and C3: SEM photomicrographs.

46.0‰) (Fig. 7). The sapropel of cycle 255 shows higher SSS values with respect to the other cycles (Fig. 7). Long term salinity trend was not observed in the studied interval. The calculated surface water density spans from 1017.8 ± 2.9 kg/m^3 to 1032.8 ± 2.9 kg/m^3, showing a similar trend and pattern of the SSS, with lower values in the sapropel (average 1023.8 kg/m^3) and higher values in the marly limestone/marlstone (average 1031.7 kg/m^3) (Fig. 4).

5. Discussions

5.1. Isotopic signature of the bulk rock

A detailed temperature and salinity reconstruction was hampered by the poor preservation of foraminifers in the marly limestone/marlstone samples. Since the isotopic signature of the bulk rock can be biased by the diagenetic calcite crystals filling and encrusting the foraminifer calcite tests (Fig. 6) (Zarkogiannis et al., 2020), to obtain reliable reconstructions we compared the isotopic composition of bulk sediment with that of calcareous nannofossils. The bulk $\delta^{18}O$ signature represents an averaged measure of all the different carbonate components present in the sediment (e.g. foraminifers, calcareous nannofossils, abiogenic calcite, dolomite, etc.). The obtained results then vary depending on the different calcite sources, which have distinct $\delta^{18}O$ offsets (Turpin et al., 2011). Dolomite, which can be characterized by different isotopic values with respect to calcite (Dela Pierre et al., 2012), is present in low abundance in the analyzed samples. However, the $\delta^{18}O$ values obtained through the treatment with phosphoric acid at 25 °C or 70 °C are similar (Fig. 4), suggesting that the $\delta^{18}O$ variations between marly limestone/marlstone and sapropel are not related to fluctuations in the dolomite contents (dolomite fully reacts with acid only at 70°C; Chaduteau et al., 2021). Diagenetic calcite crystals are rare in the sapropel, and only scattered in the marly limestone/marlstone samples where they fill foraminifer chambers (Fig. 6). Nevertheless, for these marly limestone/marlstone samples, we excluded the possible diagenetic bias of secondary calcite filling the foraminifers by analyzing the calcite fraction <45 µm, which is mostly composed of well-preserved nannofossils (Fig. 6).

The $\delta^{18}O$ values of calcareous nannofossils have been considered a more reliable proxy than the $\delta^{18}O$ of planktic foraminifers for reconstructing seawater temperature and $\delta^{18}O_{sw}$ changes (Anderson and Steinmetz, 1981). In fact, differently from planktic foraminifers, calcareous nannoplankton only proliferate within the photic zone. They do not undergo vertical migration and calcification at various depths, and their calcite platelets are more resistant to dissolution and less prone to recrystallization (Steinmetz, 1994; Subhas et al., 2018). Furthermore, previous studies showed that the $\delta^{18}O_{nannofossils}$ covaried systematically with the $\delta^{18}O_{foraminifers}$ during glacial-interglacial cycles, but with larger fluctuation amplitude, thus demonstrating the greater sensitivity of calcareous nannofossils for paleoceanographic studies (Margolis et al., 1975; Anderson and Steinmetz, 1981; Dudley and Nelson, 1989).

In order to test if the isotopic compositions of bulk calcite and of the calcareous nannofossils are comparable, the difference between the bulk and sieved samples was calculated. Furthermore, we compared the obtained differences between the bulk and calcareous nannofossils $\delta^{18}O$ values with the diversity of calcareous nannofossil assemblages, expressed in % of *U. jafari* over the whole assemblage (Fig. 4) to

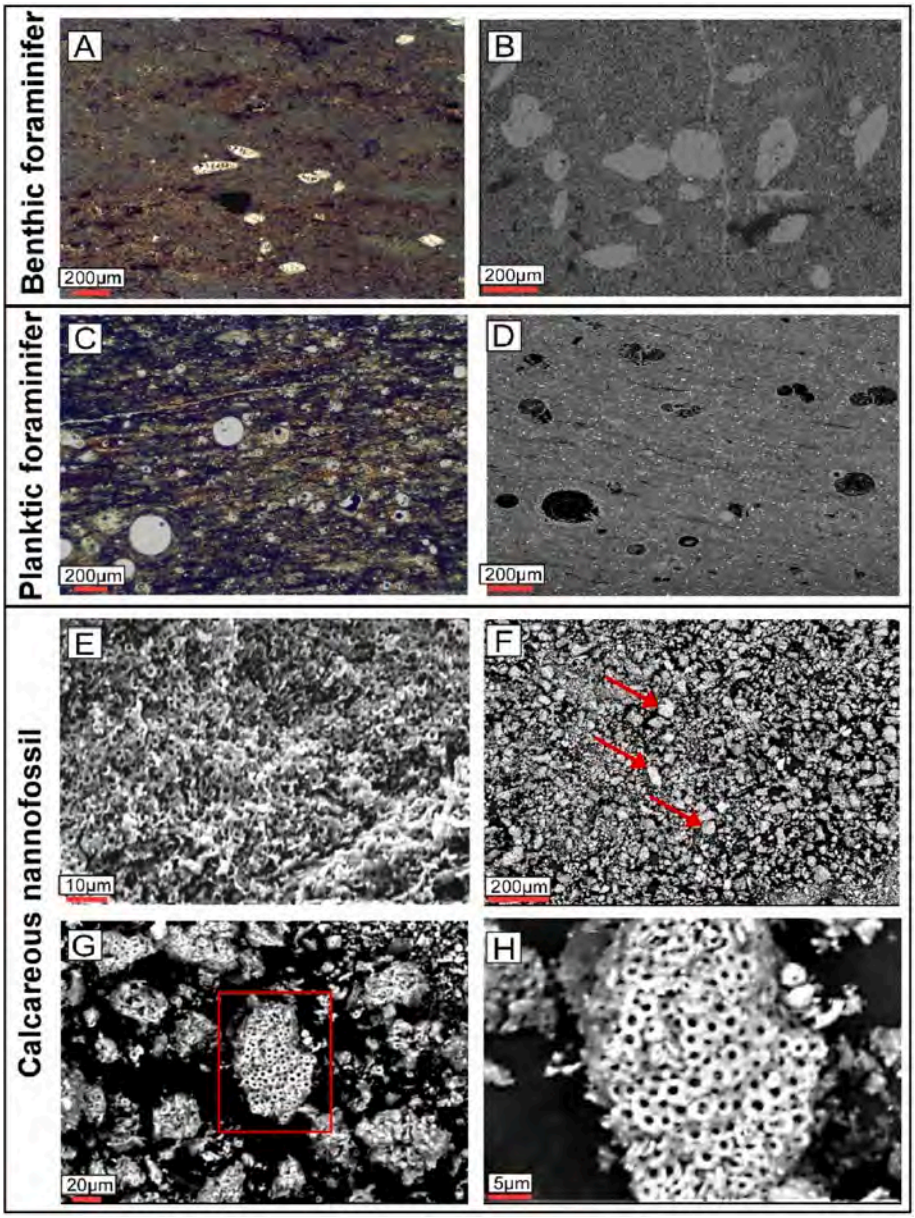

Fig. 6. Photomicrographs of representative samples in transmitted light (A and C) and SEM (B, D, E, F, G and H). A and B: Marly-limestone samples showing benthic foraminifers; calcite infill in the foraminifer chambers is visible. C and D: Sapropel sample with planktic foraminifers. E: Freshly broken sediment chip showing fecal pellet composed of monospecific assemblage of *U. jafari*. F: Sample sieved at 45 µm (red arrows indicate the fecal pellets rich in calcareous nannofossils), G: Detail of F; the red square indicates the image in H. Note the well-preserved calcareous nannofossil platelets.

highlight a possible bias originating from the different vital effects, characterizing different nannofossil taxa. We show that the $\Delta^{18}O$ ($\delta^{18}O_{sieved} - \delta^{18}O_{bulk}$) is positively correlated with *U. jafari* relative abundance ($R^2 = 0.8453$; Fig. 4); in other words, the isotopic difference between the sieved and bulk samples is lower as nannofossil diversity increases. This suggests that when the calcareous nannofossil assemblage is diversified, the bulk analysis reflects the calcareous nannofossil isotopic signature (0.06 ‰; Fig. 4); when the calcareous nannofossil assemblage is monospecific (>88% of the assemblage is composed by one taxon) this difference is higher (0.6‰) but anyway negligible when compared with the significant isotopic shift characterizing our cyclic record (Fig. 7). Indeed, the $\delta^{18}O$ oscillations observed from sapropel to marly limestone/marlstone are large (in some cases up to 7‰, and on average 3.3‰) and they cannot be solely explained by the different calcareous nannofossil assemblage carrying different isotopic offset. Therefore, the $\delta^{18}O_{bulk}$ variation between marly limestone/marlstone and sapropel represents a pristine signal reflecting temperature and salinity changes in the upper water column, where the calcareous nannoplankton proliferate.

5.2. The sedimentary expression of the thermohaline circulation change

The cyclic sedimentary stacking pattern observed in the analyzed section suggests recurrent changes in the oceanographic conditions of the Adriatic Basin during the Messinian.

The erosional contacts at the base of each packstone layer, which is sandwiched between sapropel and marly limestone/marlstone, indicate a hiatus. Level A is most likely the product of intense winnowing of the seafloor by bottom currents (Giresse, 2008), which washed away the fine-grained fraction leaving the sediment enriched in the sand-sized fraction at the seafloor. Prolonged sediment starvation in response to intense winnowing favored the formation of glauconite (Giresse, 2008),

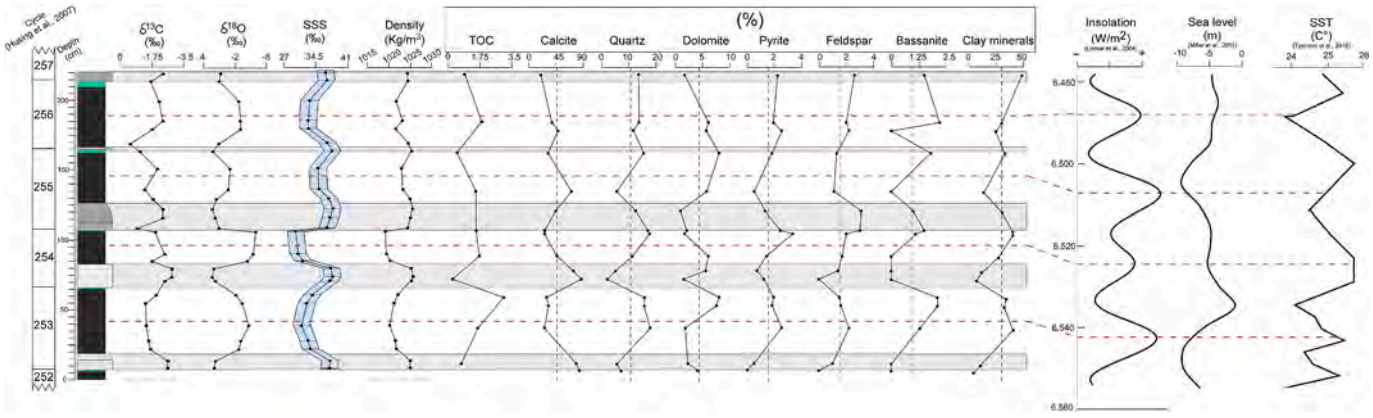

Fig. 7. Geochemical, mineralogical, stable oxygen and carbon isotope and SSS results and their relationship with the insolation curve at 45°N (Laskar et al., 2004), the global Sea level variation (Miller et al., 2011) and the alkenone-based SST measured at the Monte dei Corvi section (Tzanova et al., 2015). Vertical dashed dark lines refer to the average values, while the horizontal dashed red lines refer to the sapropel mid-points.

which is abundant in level A. These lines of evidence suggest that the packstone layers record the winnowing of the sea floor following intense bottom current activity.

The intense bioturbation of Level B suggests an oxygenated seafloor, probably favored by the resumption of thermohaline-driven bottom currents linked to precessional cyclicity. Therefore, we infer that the maximum strength of the bottom current coincides with the erosional surface at the bottom of level A, whereas the overlying parts record its slowing down.

The marly limestone/marlstone intervals exhibit frequent lamination, with occasional burrows and abundant benthic foraminifers. Specifically, the benthic foraminifer community is primarily composed of elongated biserial and triserial taxa (Iaccarino et al., 2008; Di Stefano et al., 2010), which are adapted to thrive in oxygen-depleted environments with high carbon supply to the seafloor. Notably, bolivinids, buliminids and uvigerinids (Murray, 2006; Schumacher et al., 2007) are prominent among these taxa. The reduced oxygen levels in this setting have led to intermittent crises in the benthic ecosystem, allowing only benthic foraminifers capable of tolerating sub-oxic bottom conditions to survive. These conditions also favored the preservation of undisturbed lamination.

The sapropel layers suggest a further reduction in the bottom oxygen content, which is highlighted by the decrease in abundance of benthic foraminifers, the complete absence of bioturbation, and higher pyrite and terrigenous contents compared with the marly limestone/marlstone (Fig. 7). The small size (<10 μm) of pyrite grains suggests anoxic conditions also in the water column (Bond and Wignall, 2010), because pyrite tends to sink when it reaches this size range. The relatively high abundance of terrigenous minerals in the sapropel is likely linked to increased runoff. These observations suggest that sapropels record the weakening, or even the stopping, of the thermohaline circulation related to enhanced runoff, as already proposed for other Messinian sapropel deposits in the Eastern Mediterranean (Schenau et al., 1999; Gennari et al., 2018).

5.3. *The causes of the deoxygenation in the Adriatic Basin during the Messinian*

Nowadays, the Eastern Mediterranean deep-sea oxygenation is provided by the North Adriatic Deep Water formation system, which mostly relies on the winter cold wind promoting a density gain of surficial waters, their sinking and thus an efficient transport of oxygen to the bottom. The Messinian deep-water renewal system of the Adriatic Basin and Eastern Mediterranean is supposed to have been similar to the modern one (Kouwenhoven and Van der Zwaan, 2006). After 6.7 Ma there is evidence of thermohaline circulation weakening in response to the tectonic restriction of the Atlantic gateways (Kouwenhoven et al., 2003; Sierro et al., 2003; Bulian et al., 2022), leading to enhanced sapropel formation. Instead, to the best of our knowledge, the cyclical occurrence of packstone layers related to intense bottom current activity has never been reported in the pre-evaporitic Messinian succession of the Adriatic Basin (Kouwenhoven et al., 1999; Manzi et al., 2007). In this perspective, the Monte dei Corvi section was probably located in a strategic site, intercepting the paleo-North Adriatic Deep-water path and therefore, recording variations in its strength. Despite the absolute values of the obtained SSS should be taken with caution because they can be affected by a large uncertainty (see paragraph 3.2), the obtained trend is reliable and allows to investigate the behavior of the thermohaline circulation during the Messinian. Our SSS evaluation shows that sapropels were deposited on average with SSS of 35.6‰ and with SST of 25.1 °C (Fig. 7). The corresponding surface water density estimation spans from 1017.8 to 1027.3 kg/m^3 (average 1023.8 kg/m3) (Table 1). Thus, these values are retained as indicative of the suppression of bottom water formation and consequent oxygen delivery to the sea floor, allowing the preservation of organic-rich sediments (Fig. 8). The density values during sapropel formation (Fig. 4) are lower than those of the modern Mediterranean, which is on average 1028 kg/m^3 (Droghei et al., 2018), and 1029.2 kg/m^3 in the Adriatic Sea (Gačić et al., 2001); these values allow deep-water formation events. Therefore, if in the near future under the influence of global warming, surface density values become similar to the Messinian sapropel, thermohaline circulation is likely to be negatively affected, possibly resulting in the establishment of bottom anoxic conditions. Based on the reconstructed SST and SSS, the Messinian sapropel deposition at Monte dei Corvi was mostly controlled by variation in SSS (Table 1 and Fig. 7). This was probably related to increasing freshwater input into the basin in response to precession-driven climatic and oceanographic changes. Furthermore, the sensitivity of the Medietrranean Basin to freshwater input (hence SSS variation) was enhanced in response to the decreasing amount of Atlantic water entering through the paleo Gibraltar Strait.

Noteworthy, another important parameter in the consumption of oxygen at the seafloor is the remineralization of pelagic rain of organic carbon (Burdige, 2007; Keeling et al., 2010). The amount of organic carbon reaching the sea floor depends on a wide array of factors (e.g. oxygen content, remineralization and sedimentation rate, type of organic matter, etc.; Burdige, 2007); among them, the surface primary productivity exerts the most important role. The Quaternary and Pliocene sapropels are thought to have been deposited under the joint effect of the deterioration of the thermohaline circulation and of an increase in marine productivity, both provided by enhanced river runoff from the Nile River (Triantaphyllou et al., 2009; Hennekam et al., 2014; Athanasiou et al., 2017; Blanchet et al., 2021; Mancini et al., 2023). Although

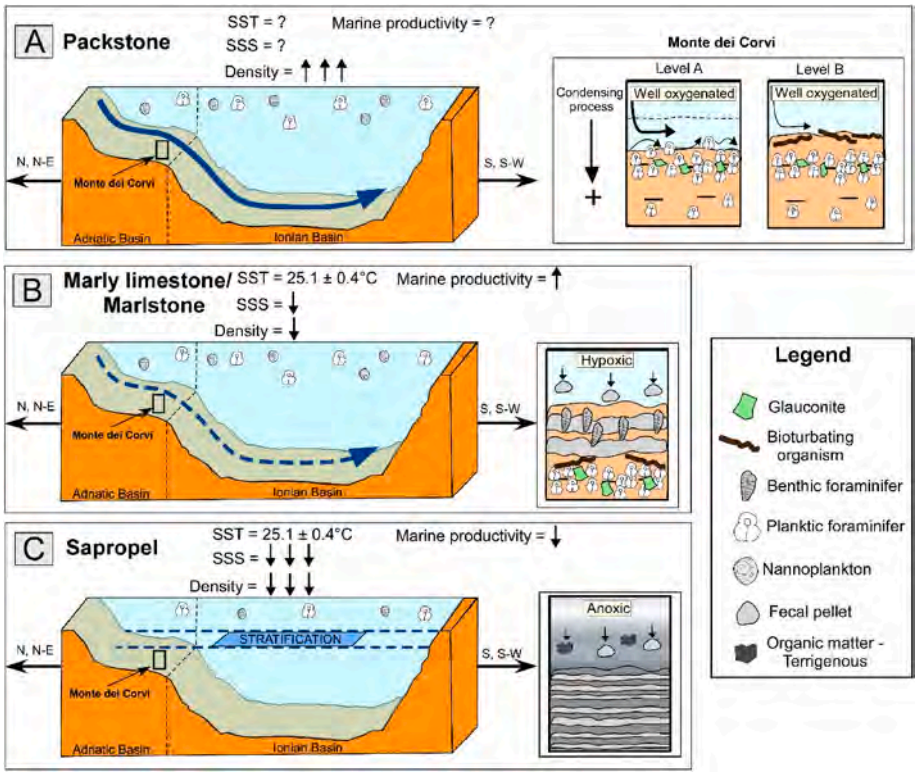

Fig. 8. Sketch showing a N-NE to SSW oriented section of the Adriatic and Ionian basins with the main oceanographic processes characterizing the deposition of the different lithologies. The main sedimentary features at Monte dei Corvi are shown in the right panels. The blue arrows represent the Adriatic Deep Water formation system with the reconstructed SST and the deducted SSS and density of surface water (this work; Tzanova et al., 2015).

our dataset does not allow for a quantitative assessment of marine productivity, from a micropaleontological and sedimentological perspective it can be inferred that the high abundance of fecal pellets, primarily composed of monospecific and/or oligospecific nannofossil taxa (*U. jafari*) in the marly limestone/marlstone layers, is indicative of enhanced primary productivity in the water column, with subsequent export to the seafloor. A similar interpretation of *U. jafari* paleoecological preference was proposed also for other Messinian sedimentary successions from the Mediterranean region (e.g., Lozar et al., 2018; Pellegrino et al., 2020).

In contrast, such evidence is absent in the sapropel layers, suggesting that their deposition was characterized by lower primary productivity and export in comparison to the marly limestone/marlstone layers. It is important to note that the deposition of the marly limestone/marlstone layers occurred under higher surface water density conditions compared to present-day conditions (Table 1). This higher density would have facilitated effective renewal of oxygen at the bottom consequently, the hypoxic conditions inferred from the marly limestone/marlstone layers can be attributed to enhanced productivity and subsequent export to the seafloor, which promotes high consumption of oxygen during organic matter remineralization. Such reconstruction suggests that primary productivity and export played a significant role in regulating the oxygen budget at the seafloor during the deposition of the marly limestone/marlstone layers. Conversely, the deposition of the sapropel layers was predominantly influenced by a weakening of the thermohaline circulation, resulting from the freshening of the upper part of the water column.

5.4. *The Messinian deoxygenation dynamics: insight for the end of this century*

Understanding past anoxic events is pivotal to tackle the future evolution of the marine environment in a global context of climate change. Indeed, the results obtained in this study testify the negative repercussions of reduced bottom oxygen levels on the seafloor ecosystem, a condition that is currently occurring in several marine sites (Diaz and Rosenberg, 2008). Seafloor deoxygenation not only involves the disappearance of complex (i.e. multicellular) organisms in the lower part of the water column and at the sediment/water interface, but likely affects also the biocenosis proliferating in the upper water column, as observed in modern environments where hypoxic/anoxic conditions establish on the seafloor (Roman et al., 2019 and references therein). As a modern example, in Elefsina Bay (Eastern Mediterranean), the development of seasonals hypoxic zone at the bottom reduces the trophic transfer energy toward the surface, thus impacting the plankton structure and favoring picoeukaryotes over mesozooplankton (Batziakas et al., 2020), hence influencing the zooplankton and fish stock (Roman et al., 2019).

The Messinian record can provide clues to better understand some of the current deoxygenation cases as it was characterized by the progressive restriction of the Mediterranean Basin in response to a reduced connection with the Atlantic Ocean through the paleo-Gibraltar Strait (Kouwenhoven et al., 1999); these conditions caused the excellent record of environmental change in the Mediterranean sedimentary succession (Kouwenhoven et al., 2003; Mancini et al., 2020), especially for the variation in the thermohaline circulation regime (Kouwenhoven and Van der Zwaan, 2006). Indeed, the SST and SSS play a major role in controlling the density of water and, therefore, on the thermohaline circulation strength. However, modeling the future thermohaline circulation behavior based on SSS and SST is complicated. Although there is a general consensus on the weakening of thermohaline circulation at the end of this century (Somot et al., 2006; Planton et al., 2012; Powley et al., 2016), some studies show that this behavior depends on the imposed boundary conditions, such as the river runoff flux (Adloff et al., 2015). Therefore, it is crucial to establish the boundary conditions at the sea surface affecting thermohaline circulation and, consequently, bottom deoxygenation. In this perspective, the Messinian sedimentary

record of the Mediterranean region is ideal to constrain the boundary condition (SST and SSS threshold) involved in the deterioration of the thermohaline circulation strength under extreme paleoceanographic stress.

The climatic conditions during the Messinian represent a valuable analog for the next future scenario because of similar SST. Tthe SST recorded in the Eastern Mediterranean during the studied interval spans from 22 °C to 30 °C (Mayser et al., 2017; Vasiliev et al., 2019; Kontakiotis et al., 2022; Butiseacă et al., 2022), and from 24.4 °C to 25.7 °C in the Monte dei Corvi section (Tzanova et al., 2015) (Table 2). The SST ranges are attributed to variation in the available insolation driven by precession. These values are higher than the modern ones, which span from 17 °C to 19 °C in the period 1986–2015 in the Northern Adriatic, and from 20 °C to 22.5 °C in the Levantine and Ionian seas (Sakalli, 2017). However, using linear black box model, the SST predicted for the period 2071–2100 (20 °C–21 °C in the Northern Adriatic; 23 °C–26 °C in the Levantine and Ionian seas; Sakalli, 2017) is close to the range of the SST reconstructed for the Messinian from 6.6 to 6.4 Ma in the Eastern Mediterranean (Tzanova et al., 2015; Mayser et al., 2017; Vasiliev et al., 2019; Kontakiotis et al., 2022; Butiseacă et al., 2022).

Predictions based on Regional Climate System Models, on multi-scenario emission approach, show that with "business as usual" greenhouse gases emission (Representative Concentration Pathways 8.5, referred to as RCP8.5 scenario), the SST will be in the range of 20.1 °C–22.3 °C in the Northern Adriatic, and between 22.5 °C–25.9 °C in the Levantine and Ionian seas at the end of this century (Darmaraki et al., 2019). The general warming trend will be accompanied by increasing surface salinity, on average of 0.48 psμ for the whole Mediterranean (Somot et al., 2006). The comparison of the Messinian SST (Tzanova et al., 2015) and the reconstructed SSS with the projected values for the end of this century in the Adriatic Sea show that the boundary conditions for bottom deoxygenation in response to reduced thermohaline circulation strength will not be reached. This is mostly because the projected increase in SSS counteracts the density loss by warming (Somot et al., 2006). Furthermore, the freshwater input from the Nile River, which was the main driver for the surface water buoyancy loss during past deoxygenation events (Rohling et al., 2015), almost stopped after the building of the Aswan dam (Rohling and Bryden, 1992). This apparently suggests that, sapropels will not be deposited on the Mediterranean seafloor in the next future in response to a reduced density of the surface water (Mancini et al., 2023). Nevertheless, it is important to consider that the deep-water renewal system in the Eastern Mediterranean essentially relies on cold wind blowing during winter (Rohling et al., 2015); thus, the thermohaline circulation strength and the deep-water renewal system are also controlled by the winter SST in the Northern Adriatic and Levantine seas, although the role of the Aegean Sea could be relevant in certain conditions (Roether et al., 1996; Incarbona et al., 2016). The resolution of our study (century/millennia) is not sufficient to evidence interannual variability and seasonal variations, like for instance the heatwaves phenomena. In the modern setting, heatwaves are currently increasing and are predicted to further increase in the Mediterranean Basin (Darmaraki et al., 2019; Garrabou et al., 2022) and could severely affect the thermohaline circulation, especially if they occur in winter. Furthermore, the weakening of the thermohaline circulation is occurring simultaneously with coastal eutrophication, which is contributing to oxygen depletion in various marginal sites within the Mediterranean (Diaz and Rosenberg, 2008). Although continental runoff is expected to decrease even further in the near future (Somot et al., 2006), the flushing of water in the marine realm remains nutrient-rich due to anthropogenic inputs (Diaz and Rosenberg, 2008). These substances can stimulate marine primary productivity, leading to oxygen loss. If this fertilization of the marine environment extends to distal areas, the resulting oxygen consumption from this process could be significant also in the deep-water setting. Therefore, all these additional forcing should be also considered in the model-based projection of the Mediterranean oxygen balance, and a hypoxic future of the Mediterranean cannot be excluded.

Table 2
Sea surface temperature recorded in the Eastern Mediterranean during the Messinian (~6.6–6.4Ma) and the projected SST from 2071 to 2100 period.

Reference	SST (C°)	Site	Proxy
	From 6.6 to 6.4 Ma		
Butiseacă et al. (2022)	27.2–30	Agios Myron (Greece)	TEX_{86}; U^{k}_{37}
Kontakiotis et al. (2022)	27.2–30	Agios Myron (Greece)	TEX_{86}; U^{k}_{37}
Mayser et al. (2017)	22–29.8	Pissouri (Cyprus)	TEX_{86}
Vasiliev et al. (2019)	22–23.4	Kalamaki (Greece)	U^{k}_{37}
Tzanova et al. (2015)	24.0–26.0	Monte dei Corvi (Italy)	U^{k}_{37}
/	**From 2071–2100**	/	**Model**
Sakalli (2017)	20–21	Northern Adriatic	Black box model
Sakalli (2017)	23–26	Levantine and Ionian	Black box model
Darmaraki et al. (2019)	20.1–22.3	Northern Adriatic	Regional climate system (RCP8.5)
Darmaraki et al. (2019)	22.5–25.9	Levantine and Ionian	Regional climate system (RCP8.5)

6. Conclusions

During the Messinian, the Monte dei Corvi section was located in or near the Adriatic Deep Water formation site and recorded variations in its intensity. Indeed, the lithological alternation made up of packstone, marly limestone/marlstone and sapropel, reflects variation in the Adriatic Deep Water formation system. The packstone layers overlying the sapropel beds were deposited under protracted bottom current activities and represent the (precession-induced) cyclical maximum strength of the thermohaline circulation, which resulted in the periodical restoration of a well-oxygenated bottom environment. As testified by the benthic foraminifer assemblage, the marly limestone/marlstone was deposited under bottom hypoxic conditions, which diminished the proliferation of bioturbating organisms. The sapropels are characterized by the absence of bioturbation and scarce benthic foraminifers, thus reflecting an ecological crisis affecting the deep ecosystem due to anoxic conditions.

Anoxic conditions during sapropel deposition were not primarily related to an intensification of marine productivity but were achieved with an increase in the buoyancy of the surficial water mass, primarily promoted by a decrease in the SSS, which in turn weakened the thermohaline circulation strength and promoted bottom anoxic conditions.

Through a comparison of the Messinian climatic and oceanographic conditions with the projected scenarios for the end of this century in the Mediterranean Basin, this study suggests that the seafloor will continue to receive sufficient oxygen due to the compensatory effect of the increased SSS, which counteracts the density loss caused by warming. Despite this, an evaluation of the role of primary productivity and heatwaves is necessary for providing reliable forecasts of the oxygen balance fluctuations in marine environments in the next future.

Declaration of competing interest

The authors declare no conflict of interest.

Data availability

Data will be made available on request.

Acknowledgment

This project was supported by CRT (Cassa Risparmio Torino) grant 2021.0907 awarded to Francesca Lozar.

Appendix A. Supplementary data

Supplementary data to this article can be found online at https://doi.org/10.1016/j.dsr.2023.104217.

References

Adloff, F., Somot, S., Sevault, F., Jordà, G., Aznar, R., Déqué, M., Herrmann, M., Marcos, M., Dubois, M., Padorno, E., Alvarez-Fanjul, E., Gomis, D., 2015. Mediterranean Sea response to climate change in an ensemble of twenty first century scenarios. Clim. Dynam. 45, 2775–2802.

Anderson, T.F., Steinmetz, J.C., 1981. Isotopic and biostratigraphical records of calcareous nannofossils in a Pleistocene core. Nature 294, 741–744.

Athanasiou, M., Bouloubassi, I., Gogou, A., Klein, V., Dimiza, M.D., Parinos, C., Skampa, E., Triantaphyllou, M.V., 2017. Sea surface temperatures and environmental conditions during the "warm Pliocene" interval (~ 4.1–3.2 Ma) in the Eastern Mediterranean (Cyprus). Global Planet. Change 150, 46–57.

Athanasiou, M., Triantaphyllou, M.V., Dimiza, M.D., Gogou, A., Panagiotopoulos, I., Arabas, A., Skampa, e., Kouli, M., Tsiolakis, E., 2021. Reconstruction of oceanographic and environmental conditions in the eastern mediterranean (Kottafi Hill section, Cyprus island) during the middle Miocene climate transition. Rev. Micropaleontol. 70, 100480.

Batziakas, S., Frangoulis, C., Tsiola, A., Nikolioudakis, N., Tsagaraki, T.M., Somarakis, S., 2020. Hypoxia changes the shape of the biomass size spectrum of planktonic communities: a case study in the eastern Mediterranean (Elefsina Bay). J. Plankton Res. 42, 752–766.

Bertini, A., Menichetti, E., 2015. Palaeoclimate and palaeoenvironments in central Mediterranean during the last 1.6 Ma before the onset of the Messinian Salinity Crisis: A case study from the Northern Apennine foredeep basin. Rev. Palaeobot. Palynol. 218, 106–116.

Blanchet, C.L., Tjallingii, R., Schleicher, A.M., Schouten, S., Frank, M., Brauer, A., 2021. Deoxygenation dynamics on the western Nile deep-sea fan during sapropel S1 from seasonal to millennial timescales. Clim. Past 17, 1025–1050.

Bond, D.P., Wignall, P.B., 2010. Pyrite framboid study of marine Permian–Triassic boundary sections: a complex anoxic event and its relationship to contemporaneous mass extinction. Bulletin 122, 1265–1279.

Bulian, F., Kouwenhoven, T.J., Jiménez-Espejo, F.J., Krijgsman, W., Andersen, N., Sierro, F.J., 2022. Impact of the Mediterranean-Atlantic connectivity and the late Miocene carbon shift on deep-sea communities in the Western Alboran Basin. Palaeogeogr. Palaeoclimatol. Palaeoecol. 589, 110841.

Burdige, D.J., 2007. Geochemistry of Marine Sediments. Princeton university press.

Butiseacă, G.A., van der Meer, M.T.J., Kontakiotis, G., Agiadi, K., Thivaiou, D., Besiou, E., Antonarakou, A., Mulch, A., Vasiliev, I., 2022. Multiple crises Preceded the mediterranean salinity crisis: Aridification and Vegetation changes revealed by Biomarkers and stable isotopes. Global Planet. Change 217, 103951.

Chaduteau, C., Ader, M., Lebeau, O., Landais, G., Busigny, V., 2021. Organic matter removal for continuous flow isotope ratio mass spectrometry analysis of carbon and oxygen isotope compositions of calcite or dolomite in organic-rich samples. Limnol Oceanogr. Methods 19, 523–539.

Darmaraki, S., Somot, S., Sevault, F., Nabat, P., Cabos-Narvaez, W.D., Cavicchia, L., Djurdjevic, V., Li, L., Sannino, G., Sein, D.V., 2019. Future evolution of marine heatwaves in the Mediterranean Sea. Clim. Dynam. 53, 1371–1392.

De Lange, G.J., Thomson, J., Reitz, A., Slomp, C.P., Speranza Principato, M., Erba, E., Corselli, C., 2008. Synchronous basin-wide formation and redox-controlled preservation of a Mediterranean sapropel. Nat. Geosci. 1, 606–610.

Dela Pierre, F., Clari, P., Bernardi, E., Natalicchio, M., Costa, E., Cavagna, S., Lozar, F., Lugli, S., Manzi, V., Roveri, M., Violanti, D., 2012. Messinian carbonate-rich beds of the Tertiary Piedmont Basin (NW Italy): microbially-mediated products straddling the onset of the salinity crisis. Palaeogeogr. Palaeoclimatol. Palaeoecol. 344, 78–93.

Di Stefano, A., Verducci, M., Lirer, F., Ferraro, L., Iaccarino, S.M., Hüsing, S.K., Hilgen, F. J., 2010. Paleoenvironmental conditions preceding the messinian salinity crisis in the central mediterranean: integrated data from the upper Miocene Trave section (Italy). Palaeogeogr. Palaeoclimatol. Palaeoecol. 297, 37–53.

Diaz, R.J., Rosenberg, R., 2008. Spreading dead zones and consequences for marine ecosystems. Science 321, 926–929.

Droghei, R., Buongiorno Nardelli, B., Santoleri, R., 2018. A new global sea surface salinity and density dataset from multivariate observations (1993–2016). Front. Mar. Sci. 5, 84.

Dudley, W.C., Blackwelder, P., Brand, L., Duplessy, J.C., 1986. Stable isotopic composition of coccoliths. Mar. Micropaleontol. 10, 1–8.

Dudley, W.C., Nelson, C.S., 1989. Quaternary surface-water stable isotope signal from calcareous nannofossils at DSDP Site 593, southern Tasman Sea. Mar. Micropaleontol. 13, 353–373.

Flecker, R., Krijgsman, W., Capella, W., de Castro Martins, C., Dmitrieva, E., Mayser, J.P., Marzocchi, A., Modestou, S., Ochoa, D., Simon, D., Tulbure, M., van den Berg, B., van der Schee, M., de Lange, G., Ellam, R., Govers, R., Gutjahr, M., Hilgen, F., Kouwenhoven, T., Lofi, J., Meijer, P., Sierro, F.J., Bachiri, N., Barhoun, N., Alami, A. C., Chacon, B., Flores, J.A., Gregory, J., Howard, J., Lunt, D., Ochoa, M., Pancost, R., Vincent, S., Yousfi, M.Z., 2015. Evolution of the Late Miocene Mediterranean-Atlantic gateways and their impact on regional and global environmental change. Earth Science Review 150, 365–392.

Gačić, M., Lascaratos, A., Manca, B.B., Mantziafou, A., 2001. Adriatic deep water and interaction with the eastern Mediterranean Sea. In: Physical Oceanography of the Adriatic Sea. Springer, Dordrecht, pp. 111–142.

Garrabou, J., Coma, R., Bensoussan, N., Bally, M., Chevaldonné, P., Cigliano, M., Diaz, D., Harmelin, J.G., Gambi, M.C., Kersting, D.K., Ledoux, J.B., Lejeusne, C., Linares, C., Marschal, C., Pérez, T., Ribes, M., Romano, J.C., Serrano, E., Teixido, N., Torrents, O., Zabala, M., Zuberer, F., Cerrano, C., 2022. Marine heatwaves drive recurrent mass mortalities in the Mediterranean Sea. Global Change Biol. 28, 5708–5725.

Gennari, R., Lozar, F., Turco, E., Dela Pierre, F., Lugli, S., Manzi, V., Natalicchio, M., Roveri, M., Schreiber, B.C., Taviani, M., 2018. Integrated stratigraphy and paleoceanographic evolution of the pre-evaporitic phase of the Messinian salinity crisis in the Eastern Mediterranean as recorded in the Tokhni section (Cyprus island). Newsl. Stratigr. 51, 33–55.

Giorgi, F., 2006. Climate change hot-spots. Geophys. Res. Lett. 33, L08707.

Giresse, P., 2008. Some aspects of diagenesis in contourites. Dev. Sedimentol. 60, 203–221.

Gladstone, R., Flecker, R., Valdes, P., Lunt, D., Markwick, P., 2007. The Mediterranean hydrologic budget from a Late Miocene global climate simulation. Palaeogeogr. Palaeoclimatol. Palaeoecol. 25, 254–267.

Hennekam, R., Jilbert, T., Schnetger, B., de Lange, G.J., 2014. Solar forcing of Nile discharge and sapropel S1 formation in the early to middle Holocene eastern Mediterranean. Paleoceanography 29, 343–356.

Hermoso, M., 2014. Coccolith-derived isotopic proxies in palaeoceanography: where geologists need biologists. Cryptogam. Algol. 35, 323–351.

Hilgen, F.J., Aziz, H.A., Krijgsman, W., Raffi, I., Turco, E., 2003. Integrated stratigraphy and astronomical tuning of the Serravallian and lower Tortonian at Monte dei Corvi (Middle–Upper Miocene, northern Italy). Palaeogeogr. Palaeoclimatol. Palaeoecol. 199, 229–264.

Hüsing, S.K., Kuiper, K.F., Link, W., Hilgen, F.J., Krijgsman, W., 2009. The upper Tortonian–lower Messinian at Monte dei Corvi (Northern Apennines, Italy): completing a Mediterranean reference section for the Tortonian stage. Earth Planet Sci. Lett. 282, 140–157.

Iaccarino, S.M., Bertini, A., Di Stefano, A., Ferraro, L., Gennari, R., Grossi, F., Lirer, F., Manzi, V., Menichetti, E., Ricci Lucchi, M., Taviani, M., Sturiale, G., Angeletti, L., 2008. The Trave section (Monte dei Corvi, Ancona, Central Italy): an integrated paleontological study of the Messinian deposits. Stratigraphy 5, 281–306.

Incarbona, A., Martrat, B., Mortyn, P., Sprovieri, M., Ziveri, P., Gogou, A., Jordà, A., Xoplaki, E., Luterbacher, J., Langone, L., Marino, G., Rodríguez-Sanz, L., Triantaphyllou, M., Di Stefano, E., Grimalt, J., Tranchida, G., Sprovieri, R., Mazzola, S., 2016. Mediterranean circulation perturbations over the last five centuries: Relevance to past Eastern Mediterranean Transient-type events. Sci. Rep. 6, 29623.

Intergovernmental Oceanographic Commission, 2015. The International Thermodynamic Equation of Seawater–2010: Calculation and Use of Thermodynamic Properties [includes corrections up to 31st October 2015].

IPCC. Climate Change 2021: the Physical Science Basis. Contribution of Working Group I to the Sixth Assessment Report of the Intergovernmental Panel on Climate Change; Masson-Delmotte, V., Zhai, P., Pirani, A., Connors, S.L., Péan, C., Berger, S., Caud, N., Chen, Y., Goldfarb, L., Gomis, M.I., et al., Eds.; Cambridge University Press: Cambridge, UK; New York, NY, USA.

Kallel, N., Paterne, M., Duplessy, J.C., Vergnaudgrazzini, C., Pujol, C., Labeyrie, L., Pierre, C., 1997. Enhanced rainfall in the Mediterranean region during the last sapropel event. Oceanolica Acta 20 (5), 697–712.

Keeling, R.F., Körtzinger, A., Gruber, N., 2010. Ocean deoxygenation in a warming world. Ann. Rev. Mar. Sci 2, 199–229.

Kidd, R.B., Cita, M.B., Ryan, W.B.F., 1978. Stratigraphy of eastern Mediterranean sapropel sequences recovered during Leg 42A and their paleoenvironmental significance. Initial Rep. Deep Sea Drill. Proj. 42A, 421–443.

Kontakiotis, G., Butiseacă, G.-A., Karakitsios, V., Antonarakou, A., Zarkogiannis, S., Agiadi, K., Krsnik, E., Besiou, E., Zachariasse, J.-W., Lourens, L., Thivaiou, D., Koskeridou, E., Moissette, P., Mulch, A., Vasiliev, I., 2022. Hypersalinity accompanies tectonic restriction in the eastern Mediterranean prior to the Messinian Salinity Crisis. Palaeogeogr. Palaeoclimatol. Palaeoecol. 592, 110903.

Kouwenhoven, T.J., Seidenkrantz, M.S., Van der Zwaan, G.J., 1999. Deep-water changes: the near-synchronous disappearance of a group of benthic foraminifera from the Late Miocene Mediterranean. Palaeogeogr. Palaeoclimatol. Palaeoecol. 152, 259–281.

Kouwenhoven, T.J., Hilgen, F.J., Van der Zwaan, G.J., 2003. Late Tortonian–early Messinian stepwise disruption of the Mediterranean–Atlantic connections: constraints from benthic foraminiferal and geochemical data. Palaeogeogr. Palaeoclimatol. Palaeoecol. 198, 303–319.

Kouwenhoven, T.V., Van der Zwaan, G.J., 2006. A reconstruction of late Miocene Mediterranean circulation patterns using benthic foraminifera. Palaeogeogr. Palaeoclimatol. Palaeoecol. 238, 373–385.

Laskar, J., Robutel, P., Joutel, F., Gastineau, M., Correia, A.C., Levrard, B., 2004. A long-term numerical solution for the insolation quantities of the Earth. Astron. Astrophys. 428 (1), 261–285.

Lozar, F., Violanti, D., Bernardi, E., Dela Pierre, F., Natalicchio, M., 2018. Identifying the onset of the Messinian salinity crisis: a reassessment of the biochronostratigraphic tools (Piedmont Basin, NW Italy). Newsl. Stratigr. 51, 11–31.

Mancini, A.M., Bocci, G., Morigi, C., Gennari, R., Lozar, F., Negri, A., 2023. Past Analogues of deoxygenation events in the Mediterranean Sea: a Tool to constrain future Impacts. J. Mar. Sci. Eng. 11, 562.
Mancini, A.M., Gennari, R., Ziveri, P., Mortyn, P.G., Stolwijk, D.J., Lozar, F., 2020. Calcareous nannofossil and foraminiferal trace element records in the Sorbas Basin: a new piece of the Messinian Salinity Crisis onset puzzle. Palaeogeogr. Palaeoclimatol. Palaeoecol. 554, 109796.
Manzi, V., Roveri, M., Gennari, R., Bertini, A., Biffi, U., Giunta, S., Iaccarino, S.M., Lanci, L., Lugli, S., Negri, A., Riva, A., Rossi, M.E., Taviani, M., 2007. The deep-water counterpart of the messinian lower evaporites in the apennine foredeep: the fanantello section (northern Apennines, Italy). Palaeogeogr. Palaeoclimatol. Palaeoecol. 251, 470–499.
Margolis, S.V., Kroopnick, P.M., Goodney, D.E., Dudley, W.C., Mahoney, M.E., 1975. Oxygen and carbon isotopes from calcareous nannofossils as paleoceanographic indicators. Science 189, 555–557.
Mayser, J.P., Flecker, R., Marzocchi, A., Kouwenhoven, T.J., Lunt, D.J., Pancost, R.D., 2017. Precession driven changes in terrestrial organic matter input to the Eastern Mediterranean leading up to the Messinian Salinity Crisis. Earth Planet Sci. Lett. 462, 199–211.
Miller, K.G., Mountain, G.S., Wright, J.D., Browing, J.V., 2011. A 180-million-year record of sea level and ice volume variations from continental margin and deep-sea isotopic records. Oceanography 24, 40–53.
Murray, J.W., 2006. Ecology and Applications of Benthic Foraminifera. Cambridge university press.
Pellegrino, L., Abe, K., Gennari, R., Lozar, F., Pierre, F.D., Natalicchio, M., Mikami, Y., Jordan, R.W., Carnevale, G., 2020. Integrated micropaleontological study of the Messinian diatomaceous deposits of the Monferrato Arc (Piedmont basin, NW Italy): new insights into the paleoceanographic evolution of the northernmost Mediterranean region. Mar. Micropaleontol. 160, 101910.
Pilade, F., Vasiliev, I., Birgel, D., Pierre, F.D., Natalicchio, M., Mancini, A., Carnevale, G., Gennari, R., 2023. Deciphering the termination of the Messinian salinity crisis: the alkenone record of the Miocene-Pliocene transition in the northern Mediterranean. Palaeogeogr. Palaeoclimatol. Palaeoecol. 631, 111831.
Planton, S., Lionello, P., Artale, V., Aznar, R., Carrillo, A., Colin, J., Congedi, L., Duboisa, C., Elizalde, A., Gualdif, S., Hertigg, E., Jacobeit, J., Jordà, G., Li, Laurent, Mariotti, A., Piani, C., Ruti, P., Sanchez-Gomez, E., Sannino, G., Sevault, F., Somot, S., Tsimplis, M., 2012. The climate of the mediterranean region in future climate projections. In: The Climate of the Mediterranean Region. Elsevier, Oxford, pp. 449–502.
Popov, S.V., Rogl, F., Rozanov, A.Y., Steininger, F.F., Shcherba, I.G., Kovac, M., 2004. Lithological-paleogeographic maps of paratethys. CFS Cour. Forschungsinstitut Senckenberg 254, 1–46.
Powley, H.R., Krom, M.D., Van Cappellen, P., 2016. Circulation and oxygen cycling in the Mediterranean Sea: sensitivity to future climate change. J. Geophys. Res.: Oceans 121, 8230–8247.
Roether, W., Manca, B.B., Klien, B., Bregant, D., Georgopoulos, D., Beitzel, V., Kovacevic, V., Luchetta, A., 1996. Recent changes in Eastern Mediterranean deep waters. Science 271, 333–335.
Rohling, E.J., Bryden, H.L., 1992. Man-induced salinity and temperature increases in western mediterranean deep water. J. Geophys. Res.: Oceans 97, 11191–11198.
Rohling, E.J., Marino, G., Grant, K.M., 2015. Mediterranean climate and oceanography, and the periodic development of anoxic events (sapropels). Earth-Science Review 143, 62–97.
Roman, M.R., Brandt, S.B., Houde, E.D., Pierson, J.J., 2019. Interactive effects of hypoxia and temperature on coastal pelagic zooplankton and fish. Front. Mar. Sci. 6, 139.
Rossignol-Strick, M., Nesteroff, W., Olive, P., Vergnaud-Grazzini, C., 1982. After the deluge: mediterranean stagnation and sapropel formation. Nature 295, 105–110.
Roveri, M., Boscolo Gallo, A., Rossi, M., Gennari, R., Iaccarino, S.M., Lugli, S., Manzi, V., Negri, A., Rizzini, F., Taviani, M., 2005. The Adriatic foreland record of Messinian events (central Adriatic sea, Italy). Geoacta 4, 158.
Roveri, M., Flecker, R., Krijgsman, W., Lofi, J., Lugli, S., Manzi, V., Sierro, F.J., Bertini, A., Camerlenghi, A., De Lange, G., Govers, R., Hilgen, F.J., Hübscher, C., Meijer, P.T., Stoica, M., 2014. The Messinian Salinity Crisis: past and future of a great challenge for marine sciences. Mar. Geol. 352, 25–58.
Sakalli, A., 2017. Sea surface temperature change in the Mediterranean Sea under climate change: a linear model for simulation of the sea surface temperature up to 2100. Appl. Ecol. Environ. Res. 15, 707–716.
Schenau, S.J., Antonarakou, A., Hilgen, F.J., Lourens, L.J., Nijenhuis, I.A., Van der Weijden, C.H., Zachariasse, W.J., 1999. Organic-rich layers in the Metochia section (Gavdos, Greece): evidence for a single mechanism of sapropel formation during the past 10 My. Mar. Geol. 153, 117–135.
Schumacher, S., Jorissen, F.J., Dissard, D., Larkin, K.E., Gooday, A.J., 2007. Live (Rose Bengal stained) and dead benthic foraminifera from the oxygen minimum zone of the Pakistan continental margin (Arabian Sea). Mar. Micropaleontol. 62, 45–73.
Siddall, M., Rohling, E.J., Almogi-Labin, A., Hemleben, Ch, Meischner, D., Schmelzer, I., Smeed, D.A., 2003. Sea-level fluctuations during the last glacial cycle. Nature 423, 853–858.
Sierro, F.J., Flores, J.A., Ba'rcena, M.A., Vazquez, A., Utrilla, R., Zamarreno, I., 2003. Orbitally-controlled oscillations in the planktic communities and cyclical changes in western Mediterranean hydrography during the Messinian. Palaeogeogr. Palaeoclimatol. Palaeoecol. 190, 289–316.
Somot, S., Sevault, F., Déqué, M., 2006. Transient climate change scenario simulation of the Mediterranean Sea for the twenty-first century using a high-resolution ocean circulation model. Clim. Dynam. 27, 851–879.
Steinmetz, J.C., 1994. Stable isotopes in modern coccolithophores. Coccolithophores. Cambridge University Press, Cambridge, pp. 219–229.
Stratford, K., Williams, R.G., Myers, P.G., 2000. Impact of the circulation on sapropel formation in the eastern Mediterranean. Global Biogeochem. Cycles 14, 683–695.
Subhas, A.V., Rollins, N.E., Berelson, W.M., Erez, J., Ziveri, P., Langer, G., Adkins, J.F., 2018. The dissolution behavior of biogenic calcites in seawater and a possible role for magnesium and organic carbon. Mar. Chem. 205, 100–112.
Taylforth, J.E., McCay, G.A., Ellam, R., Raffi, I., Kroon, D., Robertson, A.H., 2014. Middle Miocene (Langhian) sapropel formation in the easternmost Mediterranean deep-water basin: evidence from northern Cyprus. Mar. Petrol. Geol. 57, 521–536.
Triantaphyllou, M.V., Ziveri, P., Gogou, A., Marino, G., Lykousis, V., Bouloubassi, I., Emeis, K.-C., Kouli, K., Dimizia, M., Rosell-Melé, A., Papanikolaou, M., Katsouras, G., Nunez, N., 2009. Late glacial–Holocene climate variability at the south-eastern margin of the Aegean Sea. Mar. Geol. 266, 182–197.
Toby, B.H., Von Dreele, R.B., 2013. GSAS-II: the genesis of a modern open-source all purpose crystallography software package. J. Appl. Crystallogr. 46, 544–549.
Turpin, M., Emmanuel, L., Reijmer, J.J., Renard, M., 2011. Whiting-related sediment export along the middle Miocene carbonate ramp of great Bahama bank. Int. J. Earth Sci. 100, 1875–1893.
Tzanova, A., Herbert, T.D., Peterson, L., 2015. Cooling Mediterranean Sea surface temperatures during the Late Miocene provide a climate context for evolutionary transitions in Africa and Eurasia. Earth Planet Sci. Lett. 419, 71–80.
Vasiliev, I., Karakitsios, V., Bouloubassi, I., Agiadi, K., Kontakiotis, G., Antonarakou, A., Triantaphyllou, M., Gogou, A., Kafousia, N., de Rafelis, M., Zarkogiannis, S., Kaczmar, F., Parinos, C., Pasadakis, N., 2019. Large sea surface temperature, salinity, and productivity preservation changes preceding the onset of the Messinian Salinity Crisis in the eastern Mediterranean Sea. Paleoceanogr. Paleoclimatol. 34, 182–202.
Zarkogiannis, S.D., Kontakiotis, G., Gkaniatsa, G., Kuppili, V.S., Marathe, S., Wanelik, K., et al., 2020. An improved cleaning protocol for foraminiferal calcite from unconsolidated core sediments: HyPerCal—a new practice for micropaleontological and paleoclimatic proxies. J. Mar. Sci. Eng. 8, 998. https://doi.org/10.3390/jmse8120998.
Ziveri, P., Stoll, H., Probert, I., Klaas, C., Geisen, M., Ganssen, G., Young, J., 2003. Stable isotope 'vital effects' in coccolith calcite. Earth Planet Sci. Lett. 210, 137–149.